EVALUATION OF INTERMETALLIC REACTION LAYER FORMATION WITHIN STEEL ENCAPSULATED METAL MATRIX COMPOSITES

Sean Fudger [1, 2], Eric Klier [2], Prashant Karandikar [3], Chaoying Ni [1]

[1]Department of Materials Science and Engineering, University of Delaware, 201 Du Pont Hall, Newark, DE 19716-1501, USA

[2]Army Research Laboratory Building 4600, Aberdeen Proving Ground, MD 21005, USA

[3]M Cubed Technologies, Inc., 1 Tralee Industrial park, Newark, DE 19711, USA

Keywords: Encapsulation, Metal Matrix Composite, Intermetallic, Reaction Layer

Abstract

Macro hybridized systems consisting of steel encapsulated light metal matrix composites (MMCs) deliver a low cost/light weight composite with enhanced mechanical properties. By exploiting the high strength, modulus, and damage tolerance of steels and the high stiffness and low density of MMCs the resultant macro hybridized systems alleviates the high density of steel and the poor ductility of MMCs. The resultant system, when properly designed, offers higher specific properties and a more structurally efficient system can be attained. However, the combination of these dissimilar materials, specifically iron and aluminum, often results in the formation of intermetallic compounds. In certain loading situations, these typically brittle intermetallic layers can result in degraded performance. In this research, X-ray Diffraction (XRD), X-ray Energy Dispersive Spectroscopy (EDS), and Electron Backscatter Diffraction (EBSD) are utilized to characterize the intermetallic reaction layer formed between an aluminum or magnesium MMCs reinforced with Al_2O_3, SiC, or B_4C particles and encapsulated by A36 steel, 304 stainless steel, or Nitronic® 50 stainless steel.

Introduction

A high demand exists in the aerospace, marine, and automotive industries for components which are light weight but maintain their structural integrity. Recent interest includes materials such as high strength composites, magnesium, aluminum, steel, and combinations in the form of metal matrix composites and hybrid structures [1]. Metal matrix composites have a wide range of applicability for automotive and structural applications due to the tailorability of their mechanical and physical properties [2,3]. Moreover, particulate reinforced aluminum or magnesium based MMCs with a high volume fraction of the ceramic phase provide for very high stiffness, low CTE, and low density observed in ceramics while maintaining the damage tolerance and processing advantages of cast light metals. These mechanical and physical properties can be fine-tuned by adjusting the size, distribution, or volume fraction of the reinforcement phase, utilizing different reinforcement phases, matrix alloy selection, or adjusting the processing parameters used in fabricating the MMCs [4-6]. Since cost has limited the implementation of aluminum into many automotive applications, hybrid components consisting of both aluminum and steel have drawn much attention. Joining of dissimilar metals can be performed via arc welding, spot welding, diffusion bonding, ultrasonic welding, friction stir welding, laser brazing, etc. Mechanical assembly of these materials can also be performed by using rivets [7-12]. Each process exhibits

its own limitations such as the requirement for specific filler materials, the ability to join only plate or simple geometric configurations, high cost, and/or the formation of intermetallic phases.

The steel encapsulated metal matrix composites produced for this work are formed by casting or infiltration of a molten MMC into a steel shell. The casting/infiltration processes require no additional filler material, can be incorporated into complex geometries, and are produced at a relatively low cost [13]. Inherent to the processing temperatures, hold times, and the specific steel/MMC system utilized, intermetallic regions form between the steel and MMC. These intermetallic regions can exhibit poor mechanical properties, specifically ductility, compared with the parent alloys. The Iron-Aluminum phase diagram is shown in Figure 1 with the steel/MMC encapsulation processing temperature conditions superimposed. As shown in Figure 1, the formation of each of the following intermetallic phases is possible: FeAl, FelAl$_2$, Fe$_2$Al$_5$, FeAl$_3$ (or Fe$_4$Al$_{13}$). A literature review was performed and preliminary Thermo-Calc Gibbs Free Energy predictions calculated to determine which intermetallics were most probable under these conditions.
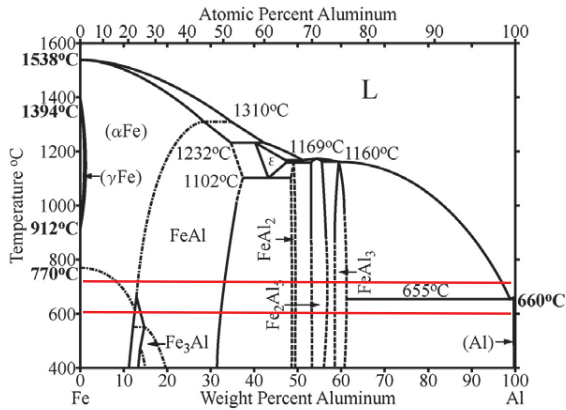
Figure 1. Iron-Aluminum Phase diagram illustrating steel/MMC encapsulation processing temperature range [13].

The formation of the intermetallic phases is driven by interdiffusion which has a direct relationship with the time and temperature history, where thicker reaction layers at the interface occur with longer time and/or higher temperature. Considerable hold times, on the order of several hours, were necessary during fabrication to guarantee the volume within the steel shell was filled completely.

Experimental Procedure

The evaluation of intermetallic reaction layers between Steel/MMC macro hybridized samples represents the main focus of this work. Steel (A36, 304, and Nitronic ® 50) bar with a diameter of greater than 0.5" was bored to produce a tube with an inside diameter of 0.188". The steel tubes were then processed to fill the internal void with various compositions of particulate MMCs,

Al-SiC, Al-Al$_2$O$_3$, and Mg-B$_4$C using a cast or infiltration approach. Finally, the gauge section of the steel/MMC bars were turned to a diameter of 0.300", 0.400" or 0.500" creating cylindrical dog-bone tensile samples as per ASTM B557-10. The various MMC cores therefore remained constant at 0.188" but with 3 different thicknesses of steel to provide for 3 different residual stress conditions. [14-19].

Table I. List of macro hybridized materials systems with resulting average reaction layer thickness.

Steel Encapsulant	Matrix Material	Reinforcement	Reinforcement percentage	Average Reaction Layer Thickness (in µm)
A36	Al-10Si	SiC	30 vol%	Max 3.5
A36	Al-10Si	SiC	55 vol%	Max 15
A36	Al-4Mg	Al$_2$O$_3$	46 vol%	250
304SS	Al-10Si	SiC	30 vol%	30
304SS	Al-10Si	SiC	55 vol%	140
304SS	Al-4Mg	Al$_2$O$_3$	55 vol%	160
Nitronic® 50	Al-10Si	SiC	55 vol%	190
Nitronic® 50	Mg AZ91E	B$_4$C	45 vol%	10

Table I presents the hybridized tensile bars produced by M-Cubed Technologies Inc. Newark DE. Two different aluminum alloys were used for the matrix material of the particulate reinforced aluminum MMCs, Al-10Si and Al-4Mg. The matrix alloys were chosen specifically for the reinforcement type in order to avoid certain thermodynamic instabilities. Since SiC tends to form Al$_4$C$_3$ when it reacts with aluminum, Al-10Si was chosen to inhibit formation of Al$_4$C$_3$ and subsequent degradation of the reinforcement particles which can drastically diminish mechanical properties [5]. An Al-4Mg alloy was selected for use with the Al$_2$O$_3$ reinforcement as this alloy provides better ductility than Al-10Si. Aluminum matrix composites were produced with SiC and Al$_2$O$_3$ particles as reinforcement at 30 and 55 vol%. An Mg AZ91E alloy was infiltrated into a bed of B$_4$C particles packed into the hollowed steel tube resulting in 45 vol% reinforcement.

Extensive characterization was performed on the tensile specimens in the form of X-ray Diffraction (XRD) and Scanning Electron Microscopy (SEM) paired with X-ray Energy Dispersive Spectroscopy (EDS) and Electron Backscatter Diffraction (EBSD). Cross sections transverse to the direction of testing, see Figure 2, were taken at multiple locations thoughout the gage section to investigate the reaction layers both within and away from the necked region after fracture. Specimens were cross sectioned using a wet diamond cut-off saw with a feed speed of 0.05 mm/s to minimize deformation.   The resulting cross-sections were mounted in Bakelite and ground with silicon carbide paper from 320 to 800 grit. Subsequently, they were polished using 3, 1, and 0.3 micron diamond slurries and final polished with 0.05 colloidal silica in a Buhler VibroMet2 vibratory polisher. This resulted in a mirror like finish which allowed for microscopic inspection of the surface.
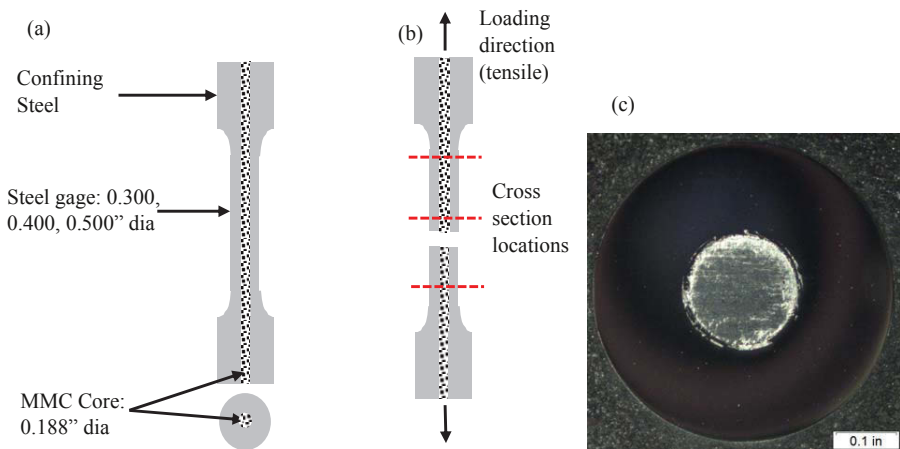
Figure 2. Design of composite tensile test sample. Illustrating (a) dimensions and material schematic (b) loading direction and typical cross section locations (c) mounted and polished cross section from 0.500" A36/Al-Al$_2$O$_3$ specimen.

XRD was performed on a Bruker D8 X-ray diffraction system in conjunction with the DIFFRAC.SUITE software. The target X-ray material was Cu with a 1.5418 angstrom wavelength operating at 40 kV and 40mA. The monochromatic Cu K$_{\alpha 1}$ line is isolated by the Vario monochromater at the X-Ray tube. A LynxEye position sensitive detector is included which permits up to 4 ° 2θ of diffracted beam to be measured continuously while scanning. A continuous 2θ scan mode was applied from 20-120° 2θ with an increment of 0.05°.

SEM analysis was performed using a Zeiss Auriga 60 Crossbeam^{TM} FIB-SEM to study reaction zones, particle size, and distribution. Furthermore EDS and EBSD were performed utilizing the Oxford Aztec software. Line, area, and map scans were created covering the reaction layers of each hybrid material. Quantitative results were obtained and cross referenced with measured XRD peaks to aid in properly identifying intermetallic formation. Electron Backscatter Diffraction was utilized for phase identification at the interface.

Results and discussion

XRD was performed on the interface between each of the hybridized materials systems. Each system consists of a unique combination of steel and MMC resulting in considerably different reaction layers based on the interaction of the constituents. Table II shows the elemental composition of the steels and MMC matrix alloys used in this work. As evident from table II, significant amounts of alloying elements are present, specifically Chromium, Nickel, and Manganese, within the stainless steels. Although the focus of this paper is on the formation of Fe-Al intermetallics, future effort will include identifying and characterizing all intermetallic phases present in the hybridized materials systems.

Table II. Steel and matrix alloys utilized within the steel encapsulated metal matrix systems.

Element	A36	304	Nitronic® 50	AZ91E	Al-4Mg	Al-10Si
Carbon	0.25 -0.29	0.08 max	0.06 max	-	-	-
Copper	0.20 max	-	-	0.003	-	0.2
Chromium	-	18.0 - 20.0	20.5 - 23.5	-	-	-
Manganese	1.03 max	2.00 max	4.0 - 6.0	0.22	-	0.1
Molybdenum	-	-	1.5 - 3.0	-	-	-
Nickel	-	8.0 12.0	11.5 - 13.5	-	-	-
Nitrogen	-	0.1 max	0.3 max	-	-	-
Phosphorus	0.04 max	0.045 max	-	-	-	-
Silicon	0.28 max	0.75 max	1.00 max	0.035	-	8.5-9.5
Sulfur	0.05 max	0.03 max	-	-	-	-
Titanium	-	-	-	-	-	0.2
Vanadium	-	-	0.10 - 0.30	-	-	-
Zinc	-	-	-	0.63	-	0.05
Aluminum	-	-	-	8.25	Balance	Balance
Iron	Balance	Balance	Balance	0.014	-	0.2
Magnesium	-	-	-	Balance	4	0.45 -0.60

Due to the variation in the reaction layer thicknesses, XRD was only able to index intermetallic phases in the hybridized materials systems which exhibit a sufficiently thick reaction layer. Figures 3 and 4 show the X-ray diffraction peaks, plotting counts vs. 2θ position, collected from the A36/Al-Al_2O_3 and Nitronic/Al-SiC systems respectively.

The X-ray tests were setup to maximize the amount of intermetallic layer area measured as compared with the surrounding materials. However, some of the adjacent material was also bombarded with x-rays and thus their peaks are present in the scans. Figure 4 shows the presence of Fe_4Al_{13} and Fe_2Al_5 at the A36/Al-Al_2O_3 interface. Some minor peaks also identify Al_2O_3 which is consistent with the reinforcement particles in the MMC. Similarly, Figure 4 shows the resultant x-ray diffraction peaks from the Nitronic-AlSiC interface, in which Fe_4Al_{13} appears to be the only intermetallic compound formed in this system.
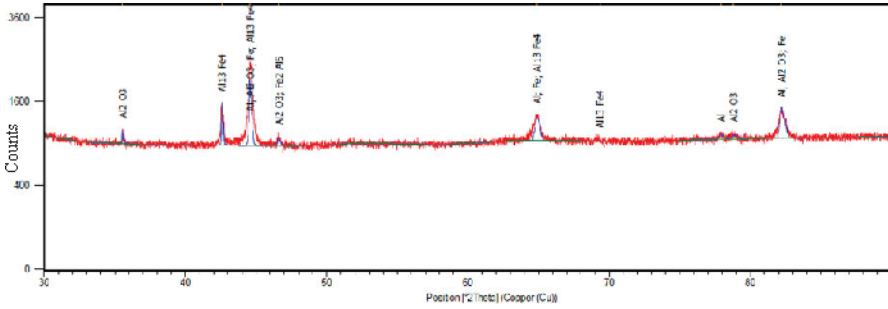
Figure 3. X-ray diffractogram A36/Al-Al$_2$O$_3$ interface.
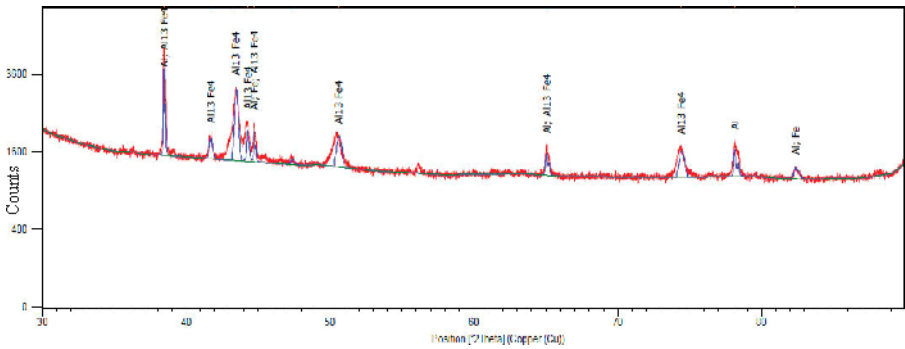
Figure 4. X-ray diffractogram of Nitronic/Al-SiC interface.

The structure of the aluminum rich phase Fe$_4$Al$_{13}$, as determined by X-ray diffraction is monoclinic, space group B2/m and with lattice parameters a= 1.5489 nm, b=0.8083 nm, c=1.2476 nm. The Fe$_2$Al$_5$ is orthorhombic, with lattice parameters a=0.7675 nm, b= 0.64030 nm, c= 0.4203 nm. The identified Fe-Al intermetallics formed, Fe$_4$Al$_{13}$ and Fe$_2$Al$_5$, are consistent with previous literature [1, 20], where Al rich phases are typically observed below processing temperatures of 1200°C and Fe rich phases above.

As evident from Figure 5, the reaction layer between the materials not only varies by thickness but also its shape. The top darker region is the MMC, the intermediate brighter region the reaction layer, and the bottom brightest region the steel in each case. The reaction layer seen in 5(a), A36 steel/Al-Al$_2$0$_3$ 46P, exhibits irregular dendritic like structure with an average thickness of about 250μm. Figure 5(b), 304 stainless steel/Al-SiC 55P, shows a much more uniform reaction layer with average thickness of about 170μm. This reaction layer appears to be much more brittle as compared with (a). Figures 5c and 5d show the Nitronic/Mg-B$_4$C 45P interface. The images illustrate a reaction layer thickness of about 10μm.
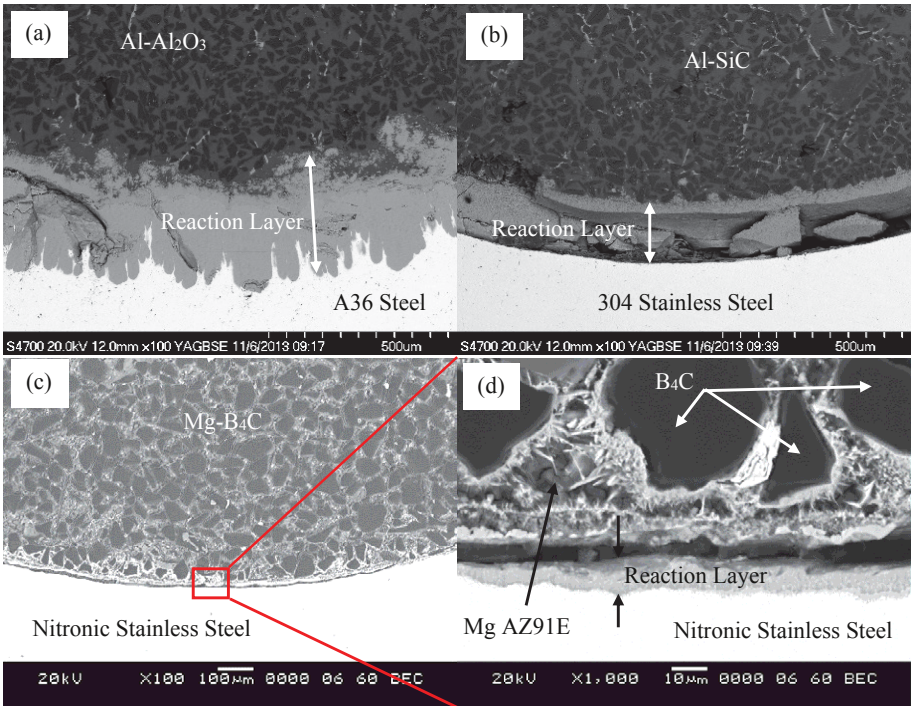
Figure 5. Backscatter electron micrographs of the interface between steel and MMC. (a) 100x magnification of A36/Al-Al$_2$0$_3$ (b) 100x magnification of 304/Al-SiC (c) 100x magnification of Nitronic/Mg-B$_4$C (d) 1000x magnification of Nitronic/Mg-B$_4$C.

The interfaces in the A36/Al-SiC 30P, A36/Al-SiC 55P, 304/Al-SiC 30P, and Nitronic/Mg-B$_4$C 45P samples varied from having no SEM detectible reaction layer to having some thin discontinuous areas of reaction thus no XRD intermetallic peaks were observed on these samples. The thinner reaction layers are likely due to the substantially shorter processing times associated with the 30P process and the fact that Mg does not react with Fe. Future efforts will make use of transmission electron microscopy (TEM) to adequately identify these minute reaction zones.

EDS and EBSD were then performed to more accurately map the intermetallic regions within the reaction layer. Due to the significant hardness difference between the multiple phases: steel, intermetallics, aluminum, and ceramic materials, substantially different material removal rates are experienced during polishing resulting in some topographical artifacts. Figure 6 shows the A36/Al-Al$_2$O$_3$ interface as imaged from an EBSD phase map. The red color on the left represents ferrite, the green section Fe$_2$Al$_5$, the yellow section Fe$_4$Al$_{13}$, and a small blue area on the right the alumina reinforcement.

Figure 6. EBSD phase map of the A36/Al-Al$_2$O$_3$ interface.

Differentiated intermetallic layers were only observed on the A36/Al-Al$_2$O$_3$ sample as the other materials only exhibit one intermetallic phase rather than the two observed here. It will be important to analyze the interfaces between the phases; steel-intermetallic interface and intermetallic-matrix interface to fully understand the macro composite properties. In addition for the A36/Al-Al$_2$O$_3$ system, the Fe$_2$Al$_5$ - Fe$_4$Al$_{13}$ interface will need to be evaluated. Future work will include quantifying the mechanical properties of these intermetallics, specifically efforts on hardness and ductility of the Fe-Al phases.

Conclusions

The intermetallic reaction layer formation of several steel encapsulated metal matrix composites was studied and characterized in this work. Specific conclusions from this research include:

1. XRD analysis and microstructural characterization suggest Fe$_2$Al$_5$ and Fe$_4$Al$_{13}$ are present in the reaction layer in the A36/Al-Al$_2$O$_3$ system. Whereas only Fe$_2$Al$_5$ are observed in the Nitronic/Al-SiC and 304/Al-SiC systems.
2. The reaction layer thickness observed in the A36/Al-Al$_2$O$_3$ system exhibits irregular dendritic like structure with an average thickness of about 250 μm.
3. The 304/Al-SiC and 304/Al-Al$_2$O$_3$ systems displays a uniform reaction layer with average thickness of about 140 μm and 160 μm respectively.
4. The A36/Al-SiC 30P, A36/Al-SiC 55P, 304/Al-SiC 30P, and Nitronic/Mg-B$_4$C 45P systems all exhibit comparatively thin, discontinuous reaction layers up to ~30 μm thick.
5. EDS and EBSD confirm the A36/Al-Al$_2$O$_3$ interface exhibits a two phase intermetallic region with a relatively smooth boundary layer between the two.

References

1. E. Taban et al. "Characterization of 6061-T6 aluminum alloy to AISI 1018 steel interfaces during joining and thermo-mechanical conditioning" Materials Science and Engineering A 527 (2010) 1704–1708.

2. A. Mazahery and M. Ostadshabani, "Investigation on mechanical properties of nano-Al_2O_3 reinforced aluminum matrix composites", Journal of Composite Materials, 45 (2011), pp. 2579-2585.

3. V. Kumar GB, Rao CSP, Selvaraj N, Bhagyashekar MS. "Studies on Al6061-SiC and Al 7075-Al_2O_3 metal matrix composites. J Miner Mater Charact Eng 2010;99(1):43-55.

4. McDaneals DL. "Analysis of stress, strain, fracture and ductility behavior of Al matrix composite containing discontinuous SiC reinforcement". Metall Trans A 1985; 16A: 1105–1115.

5. Ibrahim IA, Mohammed FA and Lavernia EJ. "Particulate reinforced metal matrix composites: a Review". J Mater Sci 1991; 26: 1137–1156.

6. Lloyd DJ. "Particle reinforced aluminum and magnesium matrix composites". Int Mater Rev 1994; 39: 1–21.

7. M. Yılmaz et al. "Interface properties of aluminum/steel friction-welded components" Materials Characterization 49 (2003) 421– 429.

8. G. Schrader et al. "Manufacturing Processes & Materials Society" Manufacturing Engineers 2000.

9. T Sakiyama et al. "Dissimilar Metal Joining Technologies for Steel Sheet and Aluminum Alloy Sheet in Auto Body" Nippon Steel Technical Report 103 May 2013.

10. A. Mathieu et al. "Laser brazing of a steel/aluminum assembly with hot filler wire (88% Al, 12% Si)" Materials Science and Engineering: A Vols 435–436, 5 November 2006, Pages 19–28.

11. O. Pasic et al. "Welding dissimilar metals – Status, requirements and trends of development" Welding in the World, 51, Pages 377-384.

12. S. Lazarevic et al. "Formation and Structure of Work Material in the Friction Stir Forming Process" Journal of Manufacturing Science and Engineering.

13. T. B. Massalski, 1986 Binary Alloy Phase Diagrams 1 ASM, 148 0-87170-261-4

14. M. Aghajanian, et al., "Processing of Hybrid structures consisting of Al-based metal matrix composites (MMCs) with metallic reinforcement of steel or titanium", TMS2013 Annual Meeting Supplemental Proceedings, John Wiley & Sons, Inc., Hoboken, NJ, (2013), 629-638.

15 P. G. Karandikar et al., "Al/Al_2O_3 MMCs and macrocomposites for armor applications," Ceramic Engineering and Science Proceedings 34 (5) (2013), 63-74.

16. P. G. Karandikar et al., "Net shape Al/B_4C metal matrix composites (MMCs) for high specific stiffness and neutron absorption applications**,"** TMS 2013 Annual Meeting Supplemental Proceedings, John Wiley & Sons, Inc., Hoboken, NJ, (2013), 683-689.

17. B. Givens, et al., "Effect of particle loading on the properties of Al/SiC metal matrix composites," in Aluminum Alloys: Fabrication, Characterization and Applications II, Yin et al. editors, TMS, Warrendale, PA (2009) 197-202.

18. P. Karandikar et al. "Metal Encapsulated MMC Macrocomposites" Materials Science & Technology 2014 Conference Proceedings.

19. S. Fudger et al. "Mechanical Properties of Steel Encapsulated Metal Matrix Composites." *Advanced Composites for Aerospace*. New York: John Wiley & Sons, 2015. 121-36. Print.

20. S. Fukumoto, et al. "Evaluation of friction weld interface of aluminum to austenitic stainless steel joint," Materials Science and Technology Volume 13, Issue 8 (01 August 1997), pp. 679-686